

# Pyroglutamylation Modulates Electronic Properties and the Conformational Ensemble of the Amyloid $\beta$ -Peptide

Justin Lemkul<sup>1</sup> and Darcy S. Davidson<sup>1</sup>

<sup>1</sup>Virginia Polytechnic Institute and State University Department of Biochemistry

November 20, 2023

## Abstract

Alzheimer’s disease (AD) is a neurodegenerative disorder that is characterized by the formation of extracellular amyloid- $\beta$  (A $\beta$ ) plaques. The underlying cause of AD is unknown, however, post-translational modifications (PTMs) of A $\beta$  have been found in AD patients and are thought to play a role in protein aggregation. One such PTM is pyroglutamylation, which can occur at two sites in A $\beta$ , Glu3 and Glu11. This modification of A $\beta$  involves the truncation and charge-neutralization of N-terminal glutamate, causing A $\beta$  to become more hydrophobic and prone to aggregation. The molecular mechanism by which the introduction of pyroglutamate (pE) promotes aggregation has not been determined. To gain a greater understanding of the role that charge neutralization and truncation of the N-terminus plays on A $\beta$  conformational sampling, we used the Drude polarizable force field (FF) to perform molecular dynamics simulations on A $\beta$ <sub>pE3-42</sub> and A $\beta$ <sub>pE11-42</sub> and comparing their properties to previous simulations of A $\beta$ <sub>1-42</sub>. The Drude polarizable FF allows for a more accurate representation of electrostatic interactions, therefore providing novel insights into the role that charge plays in protein dynamics. Here, we report the parametrization of pE in the Drude polarizable FF and the effect of pyroglutamylation on A $\beta$ . We found that A $\beta$ <sub>pE3-42</sub> and A $\beta$ <sub>pE11-42</sub> alter the permanent and induced dipoles of the peptide. Specifically, we found that A $\beta$ <sub>pE3-42</sub> and A $\beta$ <sub>pE11-42</sub> have modification-specific backbone and sidechain polarization response and perturbed solvation properties that shift the A $\beta$  conformational ensemble.

# Pyroglutamylation Modulates Electronic Properties and the Conformational Ensemble of the Amyloid $\beta$ -Peptide

Darcy S. Davidson<sup>1\*</sup> | Justin A. Lemkul<sup>1,2</sup>

<sup>1</sup>Department of Biochemistry, Virginia Tech, Blacksburg, Virginia, 24061, USA

<sup>2</sup>Center for Drug Discovery, Virginia Tech, Blacksburg, Virginia, 24061, USA

## Correspondence

Justin A. Lemkul, Biochemistry, Virginia Tech, Blacksburg, Virginia, 24061, USA  
Email: jalemkul@vt.edu

## Present address

\*Genentech, Inc.

## Funding information

National Institutes of Health, National Institute of General Medical Sciences, Grant/Award Number: R35GM133754; United States Department of Agriculture, National Institute of Food and Agriculture, Grant/Award Number: VA-160092

Alzheimer's disease (AD) is a neurodegenerative disorder that is characterized by the formation of extracellular amyloid- $\beta$  ( $A\beta$ ) plaques. The underlying cause of AD is unknown, however, post-translational modifications (PTMs) of  $A\beta$  have been found in AD patients and are thought to play a role in protein aggregation. One such PTM is pyroglutamylation, which can occur at two sites in  $A\beta$ , Glu3 and Glu11. This modification of  $A\beta$  involves the truncation and charge-neutralization of N-terminal glutamate, causing  $A\beta$  to become more hydrophobic and prone to aggregation. The molecular mechanism by which the introduction of pyroglutamate (pE) promotes aggregation has not been determined. To gain a greater understanding of the role that charge neutralization and truncation of the N-terminus plays on  $A\beta$  conformational sampling, we used the Drude polarizable force field (FF) to perform molecular dynamics simulations on  $A\beta_{pE3-42}$  and  $A\beta_{pE11-42}$  and comparing their properties to previous simulations of  $A\beta_{1-42}$ . The Drude polarizable FF allows for a more accurate representation of electrostatic interactions, therefore providing novel insights into

---

**Abbreviations:** Alzheimer's disease, AD; post-translational modification, PTM; amyloid- $\beta$ ,  $A\beta$ ; pyroglutamate, pE; force field, FF; amyloid precursor protein, APP; quantum mechanics, QM; molecular mechanics, MM; Monte Carlo/simulated annealing, MC/SA; root-mean-square deviation, RMSD; root-mean-square error, RMSE; adopted-basis Newton-Raphson, ABNR; solvent-accessible surface area, SASA

the role that charge plays in protein dynamics. Here, we report the parametrization of pE in the Drude polarizable FF and the effect of pyroglutamylation on  $A\beta$ . We found that  $A\beta_{pE3-42}$  and  $A\beta_{pE11-42}$  alter the permanent and induced dipoles of the peptide. Specifically, we found that  $A\beta_{pE3-42}$  and  $A\beta_{pE11-42}$  have modification-specific backbone and sidechain polarization response and perturbed solvation properties that shift the  $A\beta$  conformational ensemble.

#### KEYWORDS

amyloid- $\beta$ , Alzheimer's disease, post-translational modifications, pyroglutamate, polarizable molecular dynamics simulations, Drude oscillator

## 1 | INTRODUCTION

The amyloid  $\beta$ -peptide ( $A\beta$ ) is an Alzheimer's disease (AD)-associated protein that is derived from the amyloid precursor protein (APP) [1], a membrane protein believed to perform many functions [2]. APP is proteolytically cleaved by  $\beta$ -, and  $\gamma$ -secretases to form  $A\beta$  [3]. Cleavage can occur at various locations, resulting in  $A\beta$  peptides containing 36-43 amino acids [3, 4], with the most common amyloidogenic form of  $A\beta$  comprising 42 residues [5]. After  $A\beta$  is cleaved, it is released into the extracellular space, where it aggregates into oligomers and ultimately fibrils [6]. This aggregation process, and the mechanism by which oligomers convert into fibrils, is not fully understood, but mutations and post-translational modifications (PTMs) are known to accelerate aggregation [6]. Previous studies indicate that the truncation of the N- and C-termini plays a role in protein aggregation [7, 8, 9].

Several N-terminal truncations have been found in  $A\beta$  peptides from AD brains [10, 5, 11]. Here, we will discuss two N-terminal truncations, which leave Glu3 and Glu11 as the new N-termini of the peptides, which can be cyclized by glutaminyl cyclase to form N-terminal pyroglutamate (pE) residues [12, 13, 14]. Importantly, the pyroglutamylation of N-terminal residues is thought to be a driving force in protein aggregation [15]. Studies have also shown that pyroglutamylated  $A\beta$  is prevalent in AD brains [10, 15] and that the most abundant forms of  $A\beta$  in AD brains are  $A\beta_{pE3-42}$  and  $A\beta_{pE11-42}$  [16, 17]. It is also known that  $A\beta_{pE3-42}$  is cytotoxic and enhances aggregation [18]. Similarly,  $A\beta_{pE11-42}$  fibrils have also been found to be more toxic than unmodified fibrils [9]. Although we understand that these truncated, post-translationally modified species of  $A\beta$  are toxic, the atomistic details of how pyroglutamylation perturbs  $A\beta$  secondary and tertiary structure to modulate aggregation are largely unknown.

Molecular dynamics (MD) simulations have been widely employed to investigate  $A\beta$  dynamics [19, 20]. MD simulations provide atomistic insights into the dynamical behavior of proteins and how they may unfold, sample different conformations, and aggregate. Previous studies on  $A\beta$  have principally used nonpolarizable force fields (FFs), providing many useful details of how this peptide misfolds [21, 22, 23]. Gillman et al. used MD simulations to examine pE-containing  $A\beta$  pores, finding that  $A\beta_{pE3-42}$  forms ionic pores in lipid bilayers with higher conductance than pores formed by  $A\beta_{1-42}$  [23]. That study highlighted the importance of investigating how pyroglutamylation changes the electronic properties of the  $A\beta$  monomer. However, few studies have simulated pyroglutamylated  $A\beta$ , likely because

most FFs lack suitable parameters for this species. One limitation of nonpolarizable FFs is that fixed charges cannot redistribute in response to changes in their environment, which may be particularly relevant in the case of pE-containing  $A\beta$ , as it is believed to be more hydrophobic due to the loss of several charged and polar residues in its N-terminal region. To advance our understanding of pE-containing  $A\beta$  dynamics, we used the Drude polarizable FF [24, 25] to gain insight into how truncation and pyroglutamylation affect  $A\beta$  properties.

We previously performed simulations of  $A\beta$  mutants to understand the role of electronic polarization and charged amino acids in its dynamics and unfolding of a crucial central region [26]. We found that charge-altering point mutations perturb the secondary structure composition of each  $A\beta$  variant and modulate the folding free energies of a core fragment of the peptide as a function of dipole cooperativity among backbone amide groups. Furthermore, we found the interactions between the sidechain and peptide-bond dipole moments result in a hydrophobic C-terminal region (residues 29-42) that may be more aggregation-prone in the  $A\beta$  mutants. Here, we expand upon these findings by performing polarizable MD simulations of two pyroglutamylated  $A\beta_{42}$  peptides,  $A\beta_{pE3-42}$  and  $A\beta_{pE11-42}$ . Though it is known that  $A\beta_{pE3-42}$  and  $A\beta_{pE11-42}$  are found in AD brains, the extent to which pyroglutamylation modulates the monomeric  $A\beta$  conformational ensemble is unknown. Our principal goal was to understand the role that the N-terminus plays in  $A\beta$  misfolding, and how PTMs lead to shifts in secondary and tertiary structure in the earliest events along the aggregation pathway.

## 2 | METHODS

### 2.1 | Pyroglutamate Parametrization

Parametrization of pyroglutamate was performed using standard methods for the Drude FF, which have been reviewed previously [24]. Quantum mechanical (QM) geometry optimizations and dipole moment calculations were performed with the Gaussian09 program [27] and single-point interaction and configurational energies, and molecular polarizability calculations were computed with Psi4 [28]. The MP2/6-31+G\* model chemistry was used for all QM geometry optimizations, and the RIMP2/aug-cc-pVQZ model chemistry was applied for molecular polarizability, interaction energy, and single-point energy calculations, for consistency with other elements of the Drude FF [24, 25].

All molecular mechanics (MM) calculations were performed using the CHARMM program [29] with the Drude-2019 polarizable FF [25]. The initial set of coordinates for the pyroglutamate dipeptide (comprising pyroglutamate with an N-methylacetamide capping group on the C-terminus) was built using the CHARMM internal coordinate builder. After each step in the parametrization process, energy minimization was performed to compare the molecular geometry against that of the QM-optimized structure. Initial bonded and nonbonded parameter assignment was done by analogy to chemically similar groups already present in the Drude FF.

Following an initial geometry comparison, the electrostatic parameters (charges, atomic polarizabilities, and Thole screening factors) were optimized. The parameters associated with the C-terminal amide group of the pyroglutamate dipeptide were kept fixed for compatibility with the existing Drude-2019 FF. Initial parameters for other atoms and bonds were taken from the Gln and backbone parameters from Drude-2019 FF and refined using methods described in Lin et al. [25]. A Monte Carlo/simulated annealing (MC/SA) algorithm [30] was used to optimize the atomic polarizabilities and Thole screening parameters, as well as dihedral force constants. The error function was defined as the root-mean-square error (RMSE) between the QM and MM values for the quantities being fit (see below). The initial temperature was set to 500 K and was periodically scaled by a factor of 0.75 until the RMSE converged. New parameters were accepted if the RMSE decreased or if, in the case of an increase, the Metropolis criterion was satisfied at the current temperature. Convergence was defined as the RMSE difference being less than 0.001 between two

consecutive MC/SA cycles.

The target data for fitting electrostatic parameters were the QM total dipole moment,  $|\mu|$ , and its  $\mu_x$ ,  $\mu_y$ , and  $\mu_z$  components, and the total molecular polarizability ( $\alpha_{\text{iso}}$ ) and its diagonal  $\alpha_{xx}$ ,  $\alpha_{yy}$ , and  $\alpha_{zz}$  components. The Drude dipole moment and molecular polarizabilities were obtained by reading the QM optimized geometry, adding Drude oscillators and lone pairs, and relaxing the Drude oscillator positions via steepest-descent and adopted-basis Newton-Raphson (ABNR) minimization, as described by Lin et al. [25]. The gas-phase QM molecular polarizability overestimates the electric field response in solution [24, 25], so the calculated values were scaled by 0.85 for use as target data in the fitting protocol.

A key feature of the parametrization of the Drude FF is the explicit consideration of individual interactions of chemical functional groups with water, in terms of both geometry and interaction energy. These interaction energy calculations are used to tune interactions in a self-consistent manner throughout the entire FF and are used to validate and, if necessary, further optimize the electrostatic parameters derived by targeting QM dipole moment and molecular polarizability values. We assessed the interactions of water molecules placed in-plane and out-of-plane around the lactam ring of the pyroglutamate dipeptide (Figure 1). The distances between the water molecules and the pyroglutamate dipeptide functional groups were optimized via rigid QM scans in Gaussian09 [27] using the MP2/6-31+G\* model chemistry, and interaction energies were obtained in Psi4 [28] using the RIMP2/aug-cc-pVQZ model chemistry, with counterpoise correction for basis-set superposition error [31, 32].

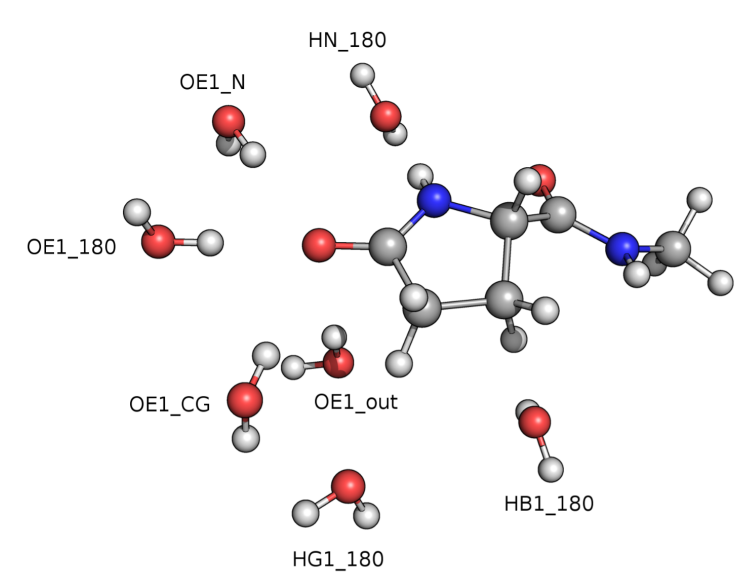


**FIGURE 1** Geometries for all water interactions with the pyroglutamate dipeptide. Each calculation was performed on a dimeric system (one pyroglutamate dipeptide and one water molecule). The composition of the image represents all the interactions that were considered as a part of the parameter validation and optimization.

One torsion in the pyroglutamate dipeptide was not previously parametrized in the Drude FF, namely N-C $\delta$ -C $\gamma$ -C $\beta$ . Starting from the QM optimized geometry, configurations were generated that set this torsion to values from  $-40^\circ$  to  $40^\circ$  in intervals of  $10^\circ$ . The geometries were optimized with this torsion frozen and all other degrees of freedom allowed to relax. Drude dihedral parameter refinement was performed with the MC/SA algorithm described above.

## 2.2 | Molecular Dynamics Simulations

*System Setup.* The starting coordinates for the full-length  $A\beta_{42}$  were obtained from the denatured WT structures produced in the simulations described in our previous work [26]. The full-length simulations, to which properties are compared here, were published in that study.  $A\beta_{pE3-42}$  and  $A\beta_{pE11-42}$  were generated by deleting residues 1-2 and 1-10, respectively. The new N-terminal Glu was patched in CHARMM to produce the pyroglutamylated N-terminus to make  $A\beta_{pE3-42}$  and  $A\beta_{pE11-42}$  using the CHARMM internal coordinate builder [29]. The C-termini of all peptides were modeled in their ionized forms. As with the full-length peptide, we simulated  $A\beta_{pE3-42}$  and  $A\beta_{pE11-42}$  in triplicate for 1  $\mu$ s each, totaling 3  $\mu$ s for each  $A\beta_{42}$  variant. All systems were initially prepared using the additive CHARMM36m (C36m) protein FF [33], then later converted to the Drude-2019 polarizable FF [24, 25] with the addition of the pyroglutamate parameters described above.

Each protein was solvated in a 72-Å cubic box of CHARMM-modified TIP3P [34, 35, 36] water and ~150 mM KCl, including  $K^+$  counterions. The systems were energy-minimized in CHARMM [29] using 1000 steps of steepest descent minimization and 1000 steps of ABNR minimization.

*Equilibration and Production Simulations.* Following minimization, equilibration was carried out in NAMD [37] for 1 ns. During equilibration, position restraints were applied to all non-hydrogen protein atoms with a force constant of 5 kcal mol<sup>-1</sup> Å<sup>-2</sup>. An NPT ensemble was maintained by regulating temperature at 310 K with the Langevin thermostat method [38, 39] using a friction coefficient,  $\gamma$ , of 5 ps<sup>-1</sup>. The pressure was set to 1 atm using the Langevin piston method [39] (oscillation period = 200 fs; decay time = 100 fs). Periodic boundary conditions were applied in all directions, and the short-range van der Waals forces were smoothly switched to zero over 10 – 12 Å. The particle mesh Ewald (PME) method [40, 41] was used to calculate the electrostatic interactions with a real-space cutoff of 12 Å and grid spacing of approximately 1 Å. Bonds to hydrogen atoms were held rigid using the SHAKE algorithm [42], allowing an integration time step of 2 fs in C36m simulations.

Following C36m equilibration, the systems were converted to the Drude polarizable model using CHARMM by adding Drude oscillators and lone pairs to the equilibrated coordinates. Additionally, the TIP3P water molecules were converted to the polarizable SWM4-NDP model [43]. Drude oscillators were relaxed using 2000 steps of steepest descent and 1000 steps of ABNR energy minimization. The Drude systems were equilibrated in NAMD using extended Lagrangian integration, implemented as Langevin dynamics [44, 45]. An NPT ensemble was maintained, and the temperature and pressure were set to 310 K and 1 atm, respectively, unless otherwise specified. Bonds involving hydrogen atoms were constrained using the SHAKE algorithm as described above.

The temperature was regulated using a dual Langevin thermostat, coupling all real atoms at 310 K ( $\gamma = 5$  ps<sup>-1</sup>) and the Drude oscillators to a low-temperature relative thermostat at 1 K ( $\gamma = 20$  ps<sup>-1</sup>). The short-range Lennard-Jones potential was switched to zero from 10 – 12 Å and electrostatic interactions were calculated with PME, using the same settings as the additive simulations. The same harmonic position restraints and bond constraints were applied as the additive simulations, but the integration time step was set to 1 fs because of the high-frequency nature of the Drude-atom bonds. To avoid polarization catastrophe, a “hard wall” constraint [46] was applied to allow a maximum Drude-atom bond length of 0.2 Å. Equilibration of polarizable systems was carried out for 1 ns. Following equilibration, the restraints were removed and the production simulations were performed in OpenMM [47, 48]. The NPT ensemble was maintained using the same thermostat settings as equilibration, except that pressure was regulated at 1 atm using a Monte Carlo barostat with box scaling attempted every 25 integration steps.

## 2.3 | Analysis

*Assessment of Convergence.* Analysis of the simulations was performed on the last 500 ns of each replicate, totaling 1.5  $\mu$ s of analyzed time for each system. Because we built the pyroglutamylated A $\beta$  systems from the starting structures described previously [26], the first 500 ns of each trajectory was characterized by considerable structural rearrangement. After 500 ns, the systems appeared to reach a point of convergence based on the root-mean-square deviation (RMSD) and radius of gyration ( $R_g$ ) (Supporting Information, Figures S1 and S2).

*Dipole Moment Analysis.* Dipole moments for peptide bonds, sidechains, and water molecules were computed using the COOR DIPOLE command in CHARMM. Each peptide bond was defined as in previous work [49], including atoms from two consecutive amino acids to define a net-neutral group. Water dipole moments were computed for any water molecule in the first solvation shell, defined as having an  $O_w$ -protein heavy atom distance  $\leq 3.5$  Å. Distance dependence was subsequently analyzed by binning these water molecules across the range of distances observed (approximately 2 Å to 3.5 Å, using a bin size of 0.1 Å). To assess the impact of each amino acid on water dipole moments, we considered only water molecules within the first solvation shell of the residue of interest and not in the first solvation shell around any other protein residue. By doing so, we ascribed the properties of the water molecules to a single amino acid.

*Structural Analysis.* Solvent-accessible surface area (SASA) of each residue was computed using the CORREL feature of CHARMM. Only real atoms were considered in the analysis (that is, Drude oscillators and lone pairs were not included). The molecular surface was computed for the entire peptide using a probe radius of 1.4 Å. Clustering of simulation snapshots was performed using the standard RMSD-based clustering methods in CHARMM as described in our previous work [26]. Tertiary structure was characterized by contact maps generated using the "gmx mdmat" program in GROMACS [50].

## 3 | RESULTS AND DISCUSSION

### 3.1 | Pyroglutamate Parametrization

To verify that the pyroglutamate topology produced good agreement with the QM electrostatic properties, the total dipole moment and molecular polarizability, and their spatial components, were calculated as described in Methods. The dipole moments and molecular polarizabilities are listed in Tables 1 and 2, respectively. The QM molecular polarizabilities in Table 2 are scaled by a factor of 0.85 for reasons described previously [24]. The optimized pyroglutamate dipeptide parameters yielded good agreement with the QM values for both the dipole moments (Table 1) and molecular polarizabilities (Table 2). We note that the errors are largest along the x-component of each of these quantities, which corresponds to the longest principal axis of the dipeptide. As only a portion of this model compound was subject to electrostatic fitting (see Methods), we accepted a small amount of error for the sake of compatibility with the remaining elements of the Drude-2019 protein FF.

Following confirmation of the dipole moments and molecular polarizabilities, the interactions of the pyroglutamate dipeptide with water (Figure 1) were calculated to further evaluate the parameters. The new pyroglutamate water interactions were in good agreement with the target QM data, in terms of both locations of energy minima and the interaction energies themselves (Table 3). The alkyl group-water interactions (HB1\_180 and HG1\_180) using the Drude FF did not adopt a stable minimum within 2.5 Å and thus the distance between the water molecules and pyroglutamate dipeptide was set to be 2.50 Å for the interaction energy calculation. This property is typical of water interactions with aliphatic groups in both the CHARMM and Drude FFs [24].

**TABLE 1** Total dipole moments and components (in D) of the pyroglutamate dipeptide.

	QM (MP2/6-31+G*)	Drude
$\mu_x$	7.05	6.21
$\mu_y$	-0.69	-1.68
$\mu_z$	1.24	0.84
$ \mu $	7.19	6.49

**TABLE 2** Components of the unscaled and scaled molecular polarizability tensors and isotropic polarizabilities ( $\text{\AA}^3$ ) of the pyroglutamate dipeptide.

	QM (RIMP2/aug-cc-pVQZ)	QM $\times$ 0.85	Drude
$\alpha_{xx}$	15.46	13.14	10.74
$\alpha_{yy}$	13.61	11.57	11.85
$\alpha_{zz}$	11.47	9.75	9.18
$\alpha_{\text{iso}}$	13.52	11.49	10.59

**TABLE 3** Water interaction energies ( $E_{\text{int}}$ , kcal mol $^{-1}$ ) and minimum-energy distances ( $r_{\text{min}}$ ,  $\text{\AA}$ ). In cases of  $r_{\text{min}} = 2.50 \text{ \AA}$  in Drude calculations, no energy minimum was identified within that distance so  $E_{\text{int}}$  was evaluated at  $2.50 \text{ \AA}$ .

	QM		Drude		Difference	
	$r_{\text{min}}$	$E_{\text{int}}$	$r_{\text{min}}$	$E_{\text{int}}$	$r_{\text{min}}$	$E_{\text{int}}$
1. OE1_180	1.98	-5.34	1.94	-6.10	-0.04	-0.76
2. OE1_out	2.07	-5.03	1.94	-6.16	-0.13	-1.13
3. OE1_CG	1.96	-6.41	1.91	-6.77	-0.05	-0.36
4. OE1_N	1.93	-6.49	1.89	-6.45	-0.04	0.04
5. HN_180	1.97	-2.65	1.99	-3.00	0.02	-0.35
6. HG1_180	2.31	-1.24	2.50	-1.18	0.19	0.06
7. HB1_180	2.26	-2.50	2.50	-2.48	0.24	0.02

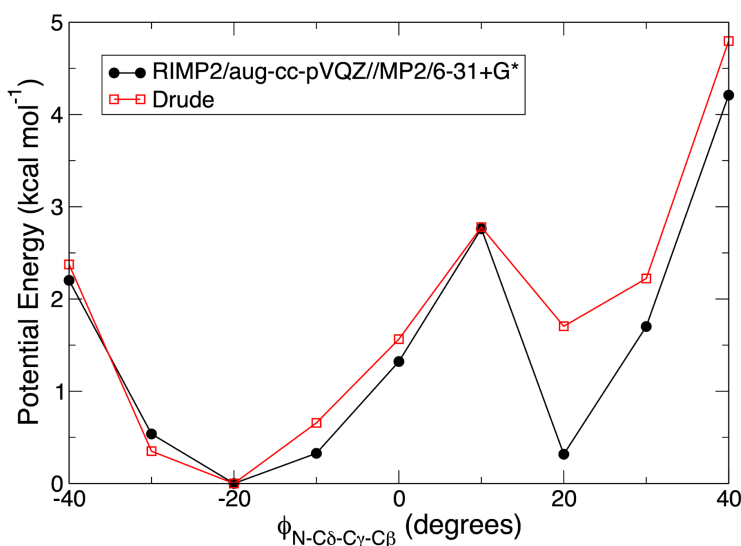


**FIGURE 2** One-dimensional potential energy surfaces as a function of the pyroglutamate dipeptide N-C $\delta$ -C $\gamma$ -C $\beta$  torsion. QM potential energies are computed using the RIMP2/aug-cc-pVQZ model chemistry following MP2/6-31+G\* optimization.

Once the dipole moments, molecular polarizabilities, and pyroglutamate water interactions were evaluated against the QM data, we analyzed the configurational energies as a function of the N-C $\delta$ -C $\gamma$ -C $\beta$  dihedral to ensure they were also in agreement with the QM data. Since the backbone parameters of most of the pyroglutamate were not adjusted as they are a core part of the FF, the only dihedral that needed to be parametrized was the angle encompassing N-C $\delta$ -C $\gamma$ -C $\beta$  (Supporting Information, Figure S3). The optimized Drude parameters for the N-C $\delta$ -C $\gamma$ -C $\beta$  dihedral produced good agreement with the QM energies (Figure 2). As such, the evaluation of all of the newly developed parameters indicated that they were sufficiently accurate for use in MD simulations. The CHARMM-formatted pyroglutamate patch and the associated parameters for it are provided in the Supporting Information.

### 3.2 | $A\beta_{pE3-42}$ and $A\beta_{pE11-42}$ Simulations

The effects of pyroglutamylation on the conformational ensemble of monomeric  $A\beta$  are not fully understood. Here, we simulated the truncated  $A\beta_{pE3-42}$  and  $A\beta_{pE11-42}$  forms of  $A\beta$  to gain a greater understanding of the role that charge alteration plays on secondary and tertiary structure, and the extent to which the truncation and modification alter the transition between helical and disordered states. Studying these truncations provides us with insight into the role that the polar N-terminal residues (particularly residues 1-10) play in  $A\beta$  misfolding. In addition, understanding the tertiary structure and contacts that are formed yields insight into how pyroglutamylation shifts the conformations in a way that impacts the aggregation pathway.

### 3.2.1 | Pyroglutamylation Shifts $\alpha$ -Helical and $\beta$ -Strand Propensity of $A\beta$

Given that interconversion between  $\alpha$ -helical and  $\beta$ -strand structures is believed to be central to the aggregation of  $A\beta$  [51], we began by comparing the  $\alpha$ -helical and  $\beta$ -strand content of  $A\beta_{pE3-42}$  and  $A\beta_{pE11-42}$ . We recently reported the secondary structural features of  $A\beta_{42}$  [26], which serve as a comparison for the present study. We did not observe any  $\beta$ -sheet content in either  $A\beta_{pE3-42}$  or  $A\beta_{pE11-42}$ . Persistent  $\beta$ -sheets are more likely in higher-order  $A\beta$  oligomers and fibrils, though we note the appearance of some short  $\beta$ -strands in our previous simulations of full-length  $A\beta_{42}$  [26]. The absence of  $\beta$ -strands here suggests that neutralization of the N-terminus and removal of several residues may impact the stability of these structures within  $A\beta_{42}$ .

We found that the  $A\beta_{pE3-42}$  had increased  $\alpha$ -helical content throughout the peptide relative to the full-length peptide, although none of these structures persisted for long periods of time (Supporting Information, Figure S4). This observation suggests that the pyroglutamylation at Glu3 results in a hydrogen bonding network that favors several short (4-5 residue)  $\alpha$ -helical turns, as compared to the unmodified  $A\beta_{42}$ , which was characterized by a single, slightly longer central  $\alpha$ -helix.  $A\beta_{pE11-42}$  was similar to  $A\beta_{42}$  in overall  $\alpha$ -helical content, as well as adopting  $\alpha$ -helical structures involving the same residues. Thus, pyroglutamylation at Glu11 may not shift the secondary structure content of  $A\beta_{42}$  as much as the modification at Glu3. This result is somewhat surprising given that the  $A\beta_{pE3-42}$  peptide has fewer residues deleted from it as a consequence of the modification, leading to an expectation that its properties would be similar to those of the unmodified  $A\beta_{42}$ . Our results suggest that deletion of the first ten residues, which are primarily charged and polar, does not substantially alter the secondary structure preferences of  $A\beta_{42}$ .

Previous work suggests that the transient formation of  $\alpha$ -helical intermediates may play a role in  $A\beta$  oligomer formation [52]. Our observations here suggest that  $A\beta_{pE3-42}$  may facilitate adoption of secondary structure elements that are "on-pathway" for  $A\beta_{42}$  aggregation, whereas  $A\beta_{pE11-42}$  may adopt an ensemble of structures that is similar to the full-length  $A\beta_{42}$  and therefore it may not differ in its propensity for aggregation, at least from the standpoint of secondary structure evolution.

We note that our results differ from those of a recent study by Nath et al. [53], who found that pyroglutamylation increased  $\beta$ -sheet in the  $A\beta_{pE3-42}$  monomer relative to  $A\beta_{42}$ ; they did not examine  $A\beta_{pE11-42}$  in their work. Their study applied replica-exchange MD simulations with the CHARMM36m nonpolarizable force field [33], so some differences may be due to the force fields applied. Nath et al. found an overall increase in  $\beta$ -sheet content in the  $A\beta_{pE3-42}$  monomer relative to  $A\beta_{42}$ , with localized increase in  $\alpha$ -helicity among residues 24-28. Here, we found no increase in  $\beta$ -strand (or sheet) content and increased helicity in residues 24-28. One aspect of the Drude polarizable force field that is important in this context is the explicit modeling of cooperative dipole induction. This effect is the reason for inadequate helix-coil equilibrium in the model (AAQAA)<sub>3</sub> peptide with CHARMM36 but proper temperature dependence with the Drude force field [54]. We have also noted the importance of dipole cooperativity in  $A\beta$  in our previous work on the unfolding of the central region of the peptide [26].

Nath et al. further noted "significantly stronger" Glu22-Lys28 and Arg5-Glu22 salt bridges in  $A\beta_{pE3-42}$  that contribute to a shifted conformational ensemble. We note that nonpolarizable force fields tend to overstate the strength of these interactions [55], which may be particularly important in amyloidogenic proteins with unusual microenvironments in which these salt bridges occur, as their properties may strongly depend on their surroundings [26].

### 3.2.2 | $A\beta_{pE3-42}$ and $A\beta_{pE11-42}$ Adopt Distinct Tertiary Structures

The contributions of secondary structure (disorder) and tertiary structure (compactness and accessibility of aggregation-prone motifs) govern the earliest events of oligomer nucleation [52, 56]. Thus, characterizing the tertiary structures

of the modified systems is crucial to our overall understanding of how truncation and modification lead to a more aggregation-prone peptide. Figure 3 shows the most representative structures from the top cluster of RMSD-based clustering for both  $A\beta_{pE3-42}$  and  $A\beta_{pE11-42}$ . Notably, the pE residue behaved differently in these species. In  $A\beta_{pE3-42}$ , the pE3 residue was buried deeply in the core of the collapsed peptide structure, surrounded by other hydrophobic residues (Figure 3A). In  $A\beta_{pE11-42}$ , the pE11 residue was exposed to solvent and the overall architecture of the peptide was more expanded than that of  $A\beta_{pE3-42}$  (Figure 3B).

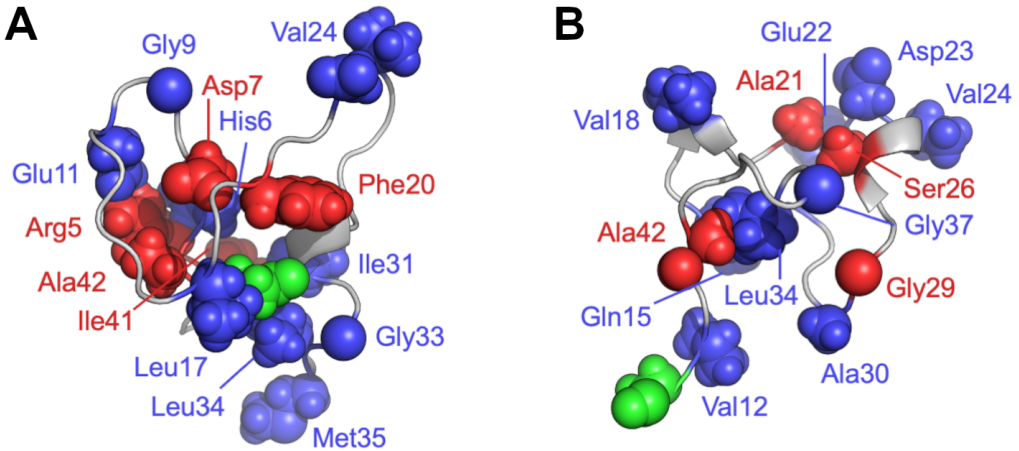


**FIGURE 3** Representative structures of  $A\beta_{pE3-42}$  and  $A\beta_{pE11-42}$  highlighting the dominant tertiary interactions seen in the  $C\alpha$ - $C\alpha$  distance matrices. Residues colored in blue are those with  $\geq 25\%$  increase in sidechain SASA and those in red are residues with  $\geq 25\%$  reduction in sidechain SASA, relative to  $A\beta_{42}$ . The green residue in both panels is pyroglutamate.

To quantitatively analyze tertiary structure, we calculated the pairwise distances between every  $C\alpha$  atom to describe the residue-residue contacts (Figure 4) and the per-residue solvent-accessible surface area (SASA). We calculated the change in SASA relative to  $A\beta$  (Figure 5). Both the  $A\beta_{pE3-42}$  and  $A\beta_{pE11-42}$  peptides had long-range contacts between N-terminal residues and those of the hydrophobic C-terminal region. The hydrophobic C-terminal residues of both  $A\beta_{pE3-42}$  and  $A\beta_{pE11-42}$  interacted with the CHC, likely driven by the residues attempting to shield themselves from the solvent and polar residues. None of these interactions were present in  $A\beta_{42}$  [26]. Correspondingly, the C-terminal region of both  $A\beta_{pE3-42}$  and  $A\beta_{pE11-42}$  had similar patterns of solvent accessibility. Residues Gly33-Gly38 were more solvent-exposed than in  $A\beta_{42}$ , whereas Val39-Ala42 were less solvent-exposed. This change in solvent accessibility occurred because the pyroglutamate interacted with residues Val40-Ala42 (Figures 3 and 4), thus shifting the Gly33-Gly38 sequence into solvent. These observations highlight that the pyroglutamylation of  $A\beta$  results in shifts in the tertiary contacts that lead to the hydrophobic C-terminal region and CHC making closer contacts in the modified systems.

In  $A\beta_{pE3-42}$ , residues Phe4, Arg5, Asp7, Ser8 were less solvent-exposed relative to the full-length peptide because of the interactions that occurred between the pyroglutamate and the hydrophobic C-terminal residues. Thus, interactions among hydrophobic groups (including the N-terminal modified residue) can therefore drive the partial burial of polar and charged residues such as Arg5, Asp7, and Ser8. The burial of the N-terminal pE3 residue in  $A\beta_{pE3-42}$

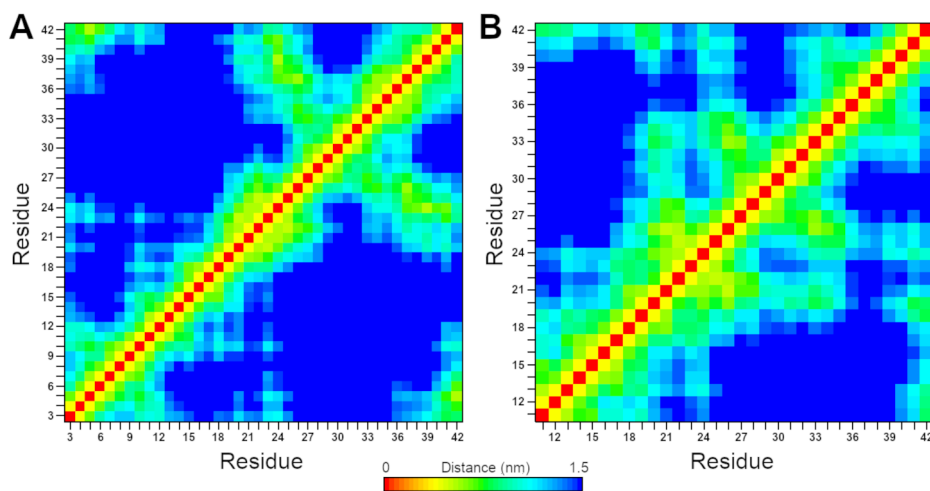


**FIGURE 4**  $\alpha$ - $\alpha$  distance matrices of (A)  $A\beta_{pE3-42}$  and (B)  $A\beta_{pE11-42}$ . All frames from the last 500 ns of each of the three replicate simulations for each system were pooled for this analysis.

caused a major reorganization of intrapeptide contacts that included the formation of an Arg5-Ala42 salt bridge (Figure 3A) that may also help stabilize this architecture. In contrast, other N-terminal residues that did not interact with the C-terminus (His6, Gly9-Val12) had increased per-residue SASA (Figure 5A). Several residues in the C-terminal hydrophobic region had increased SASA relative to  $A\beta_{42}$ , notably Leu34 and Met35.

In  $A\beta_{pE11-42}$ , His13 was less solvent-exposed than in the full-length  $A\beta_{42}$ , but the surrounding residues more solvent-exposed, most notably pE11, Val12, and Gln15 (Figures 3 and 5B). The increase in solvent accessibility of Gln15 was coupled to a burial of Ala42, with which it interacted closely (Figures 3B and 4B). The sidechain of Ala42 then packed closely with that of Leu34, defining the core of the dominant  $A\beta_{pE11-42}$  morphology. As a result, several key residues in the CHC (Leu17, Val18, and Phe20) and in the C-terminal hydrophobic region (notably Leu34) were more solvent-exposed than  $A\beta_{42}$  (Figure 5B). Taken together, the SASA results indicate that the hydrophobic residues of both  $A\beta_{pE3-42}$  and  $A\beta_{pE11-42}$  are more solvent-exposed, potentially resulting in aggregation-prone regions to interact more readily with solvent.

### 3.2.3 | Perturbation of Peptide-Bond and Sidechain Dipole Moments

Adoption of secondary structure in polypeptide chains derives from hydrogen bonding, which is a directional alignment of complementary dipoles. Tertiary structure formation is driven by packing of sidechains that subsequently define microenvironments in the folded structure. Therefore, there should be a direct connection between the structure of a polypeptide and its electrostatic properties. Alignment of peptide-bond dipoles leads to cooperative induction that ultimately gives rise to the helix macrodipole [49, 54, 57, 58], and different values of peptide-bond dipole moments are associated with specific polypeptide geometries [54]. Thus, changes in dipole moments reflect changes in structure, particularly in the case of helix-coil equilibrium, as polarization of peptide bonds will vary in response to changes in solvent exposure or the hydrogen bonding network. To relate secondary structure preferences with the electronic structure of the polypeptide backbone, we calculated the peptide-bond dipole moments of each amide group linking consecutive residues (Supporting Information, Table S1).

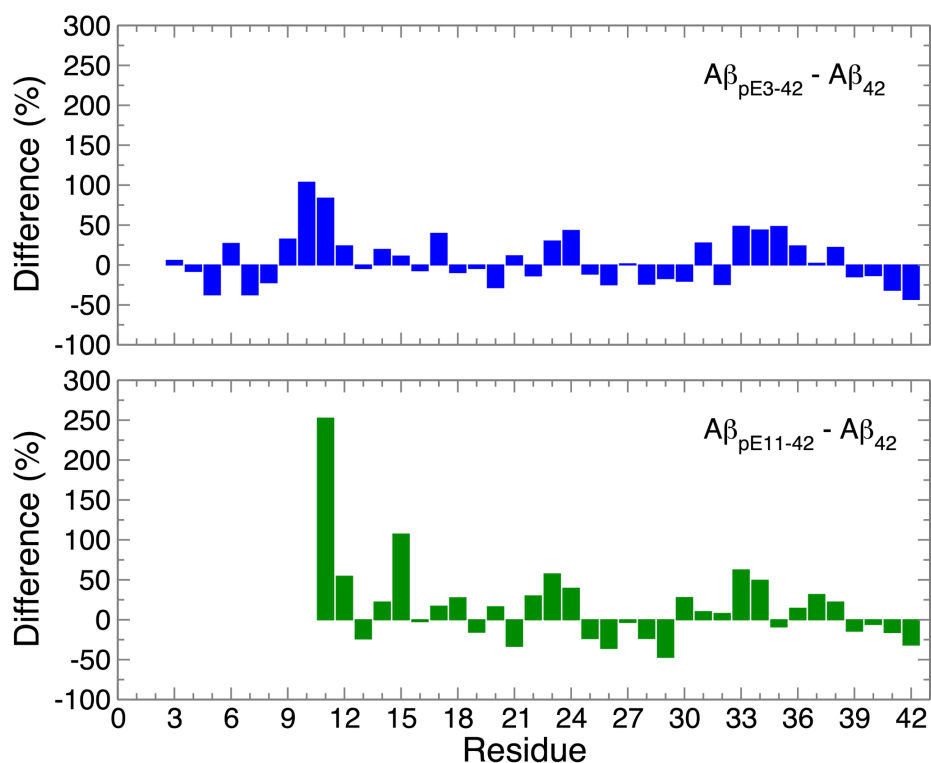


**FIGURE 5** Change in solvent-accessible surface area (SASA), expressed as a percentage difference relative to the full-length  $A\beta_{42}$  values.

The per-residue peptide-bond dipole moments of the pyroglutamylated peptides were compared against the equivalent residues of  $A\beta_{42}$ . We found that peptide bonds within the central hydrophobic cluster (CHC, residues 17–21) of both  $A\beta_{pE3-42}$  and  $A\beta_{pE11-42}$  were depolarized relative to the full-length  $A\beta_{42}$ . The decrease in peptide-bond dipole moments among CHC residues suggests that tertiary structure interactions may cause depolarization. From the analysis of inter-residue contacts (Figure 4), residues in the hydrophobic C-terminal region tended to interact with residues in the CHC. The resulting hydrophobic microenvironment is likely the reason for depolarized backbone amide groups, which were subsequently more shielded from solvent and thus accommodated their new surroundings by decreasing their dipole moments. This depolarization of the peptide bonds also suggests that pyroglutamylation weakens the hydrogen bonding network of  $A\beta$ , which leads to the depolarization of the aggregation-prone CHC.

Within the hydrophobic C-terminal region of  $A\beta_{pE3-42}$ , peptide bonds were generally depolarized relative to  $A\beta_{42}$ , with the exception of the Val36–Gly37 and Ile41–Ala42 peptide bonds. The peptide bonds spanning Gly29–Met35 and Gly38–Val40 otherwise exhibited pronounced depolarization (Figure 6). In contrast, the C-terminal region of  $A\beta_{pE11-42}$  was more polarized than  $A\beta_{42}$ , particularly among residues Val39–Ala42. This difference in dipole response was somewhat unexpected, as the levels of solvent exposure among these residues were similar between the two pyroglutamylated peptides (Figure 5). Therefore, the differences in polarization among peptide bonds reflect differences in tertiary structure and thus distinct microenvironments. As a consequence,  $A\beta_{pE3-42}$  and  $A\beta_{pE11-42}$  may undergo different unfolding pathways. Indeed, the increased polarization among the peptide bonds within Gly38–Ala42 in

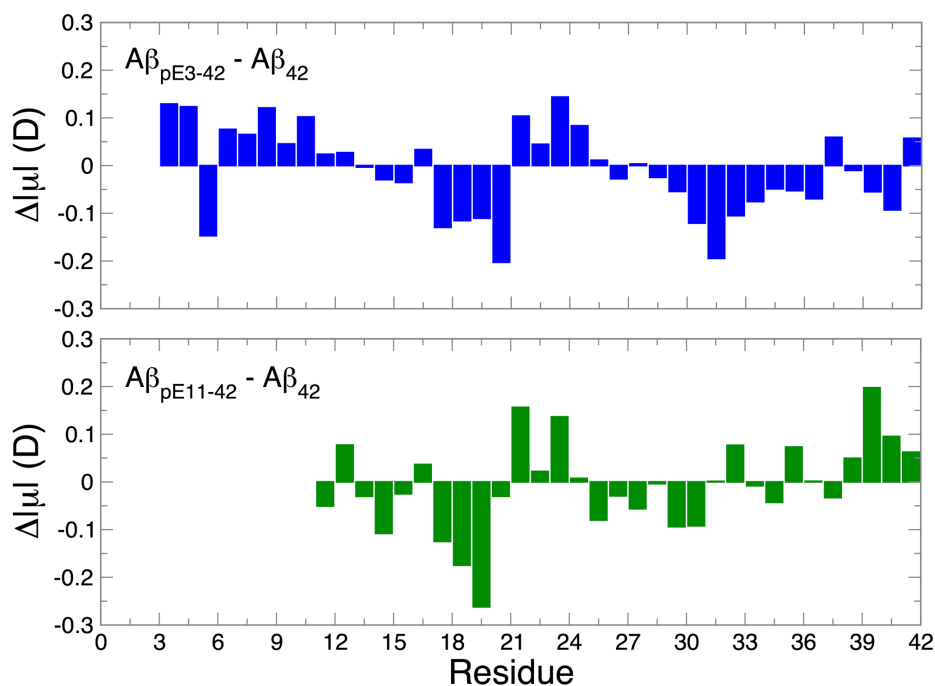


**FIGURE 6** Differences in peptide-bond dipole moments relative to  $A\beta_{42}$ .

$A\beta_{pE11-42}$  suggests that these functional groups may be more favorably solvated, contributing to disorder.

Both pyroglutamylated peptides exhibited strongly depolarized peptide bonds within the CHC. Depolarization is expected to be correlated with solvent occlusion, as the decrease in dipole moment would make these functional groups less favorably solvated. Only modest differences in SASA were observed for these residues relative to  $A\beta_{42}$ , suggesting interactions with water are similar among all three peptides. Therefore, the depolarization should be attributable to intrapeptide effects. In  $A\beta_{pE3-42}$ , the CHC residues had the largest tendency to form  $\alpha$ -helical structures, so it may be expected that the peptide-bond dipole moments would be enhanced in these residues [54]. The fact that they did not suggests that the  $\alpha$ -helical structures were somewhat weak as a function of the tertiary structure, a fact that is reflected in the preference for disordered, coil structures in this region of the peptide. The consistently depolarized nature of these amide groups strongly indicates that as a function of pyroglutamylation, these peptide bonds prefer to be shielded from water, which may be an additional driving force for their aggregation.

We then calculated the sidechain dipole moments for each residue and compared them to the  $A\beta_{42}$ . For this analysis, we omitted direct comparisons between glutamate and pyroglutamate, as well as glycine, which has no sidechain. Changes in sidechain dipole moments, expressed as percentages relative to  $A\beta_{42}$ , are shown in Figure 7. We found that the sidechain dipole moments largely followed the SASA changes (that is, residues with increased SASA resulted in larger dipole moments, and vice-versa). This parallel pattern suggests that shifts in tertiary contacts and interactions with water result in corresponding shifts in the electric field around each residue. One particularly obvious example of this phenomenon was Phe4 in  $A\beta_{pE3-42}$ , which packed against the N-terminal pyroglutamate (Figure 3); its sidechain dipole moment was strongly depolarized as a result (Figure 7). This outcome highlights that the neutralization and increased hydrophobicity of  $A\beta_{pE3-42}$  and  $A\beta_{pE11-42}$  result in changes in important microenvironments,

which subsequently manifest as shifts in sidechain dipole moments.

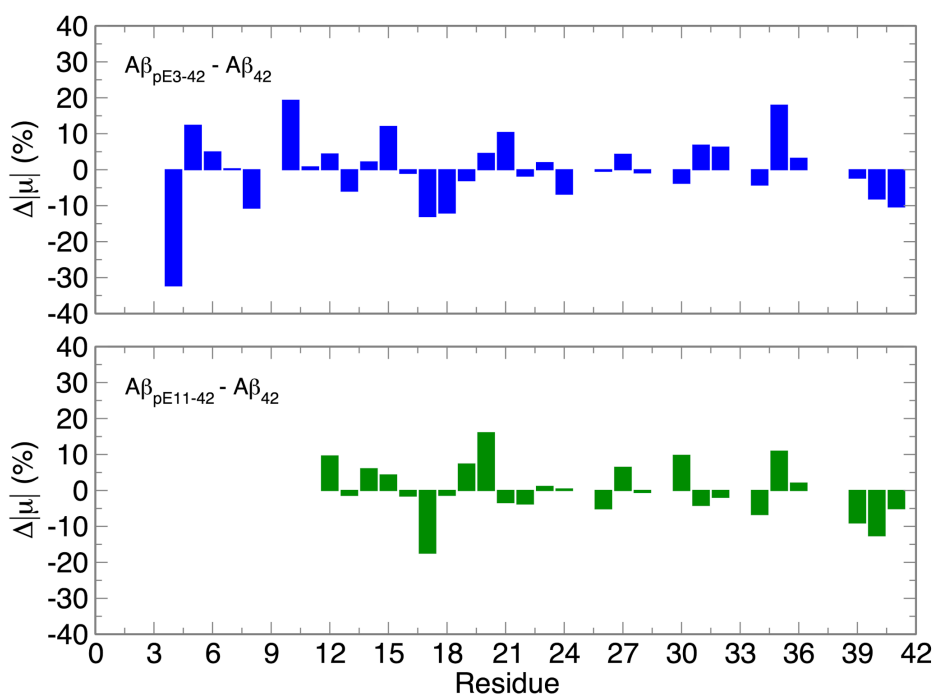


**FIGURE 7** Change in sidechain dipole moments, expressed as a percentage relative to the values of the full-length  $A\beta_{42}$  peptide. All glycine and modified residues are shown as 0% change to indicate that the comparison was not made for these residues.

### 3.2.4 | Pyroglutamylation Perturbs the Solvation Shell Around $A\beta_{42}$

The solubility of any protein or polypeptide depends, in part, on the interactions among surface-exposed amino acids and water. To understand the impact that pyroglutamylation has on the solvation shell around each  $A\beta$  peptide, we calculated the molecular dipole moments of all water molecules in the first solvation shell (heavy atom- $O_w$  distance  $\leq 3.5$  Å). We further decomposed these water molecules into those that were within the first solvation shell of each residue in the peptide but not in the first solvation shell of any other residue. Results of this analysis are shown in Figure 8.

A previous study by Ngo et al. examined the solvation properties of a model  $\alpha$ -helix and  $\beta$ -hairpin structures [59]. They found that water molecules closest to the peptide surfaces were depolarized relative to bulk water (for the SWM4-NDP model, the bulk dipole moment is  $2.47 \pm 0.16$  D [43]). The effects were greater for the  $\alpha$ -helix, which may be a function of its specific sequence. We observed a similar behavior here in the case of each of the  $A\beta$  peptides. First-shell water dipole moments around  $A\beta_{42}$  averaged  $2.43 \pm 0.16$  D, and for both  $A\beta_{pE3-42}$  and  $A\beta_{pE11-42}$ , this value was  $2.42 \pm 0.16$  D. Thus, all  $A\beta$  variants examined here behaved similarly and the observed depolarization effect was slightly smaller than what was observed by Ngo et al. By decomposing these water molecule dipole moments as a

function of distance away from the nearest peptide heavy atom, we observed a strong polarization effect ( $|\Delta\mu_{\text{wat}}| \approx 0.3 \text{ D}$ ) within  $2.5 \text{ \AA}$  (Figure 8A).  $A\beta_{42}$  had the most polarized water molecules, likely as a result of having a greater number of charged residues relative to the pyroglutamylated forms, though this effect was small (Figure 8A). Water molecules from  $2.5 - 3.5 \text{ \AA}$  away from the peptide surfaces tended to have dipole moments at, or slightly below, that of bulk SWM4-NDP.

We further sought to decompose this behavior on a per-residue level, by calculating the water dipole moments for molecules in the first solvation shell of each amino-acid residue that were not also within the first solvation shell of any other residue. Doing so will ignore residues that interact with multiple residues simultaneously but allow us to connect polarization effects among water molecules with solvent accessibility analysis described above. Results of this analysis are shown in Figure 8B. Among all the  $A\beta$  peptide variants studied here, the only residues for which observed water dipole moments were greater than the bulk water value are for acidic residues (Glu3, Glu11, Glu22, and Asp23) and the C-terminal Ala42, which is exerting this effect through its anionic C-terminal carboxylate group in  $A\beta_{42}$  and  $A\beta_{\text{pE11-42}}$ . In  $A\beta_{\text{pE3-42}}$ , Ala42 interacted strongly with Arg5 via a salt bridge (Figure 3), screening the charge on the carboxylate and leading to a slight depolarization of water molecules around the methyl sidechain. For all other residues, the water molecules were depolarized relative to bulk. Therefore, the observed polarization effects among the closest water molecules was likely due to simultaneous interactions of water with multiple  $A\beta$  residues and are difficult to describe in per-residue terms. Nevertheless, it is interesting that the closest water molecules within the first solvation shell are strongly polarized, but overall the first solvation shell is depolarized relative to bulk water.

Finally, we computed the difference in water dipole moments as a function of interaction with each residue (Figure 8C). The data shown in Figure 8C were obtained by taking the difference between the per-residue data in Figure 8B. While the magnitudes of these differences are small, they provide important context for the relationship with perturbations to SASA described above and shown in Figure 5. Given the general tendency of hydrophobic residues in the region comprising residues 30-42 of the  $A\beta_{\text{pE}}$  peptides to become more solvent exposed (Figure 5), most of their surrounding water molecules tended to depolarize in response (Figure 8B,C). Water molecules around the Glu3 and Glu11 residues were also substantially depolarized due to the fact that pyroglutamylation renders these residues uncharged and far more hydrophobic. In addition, water molecules surrounding the CHC were generally among the most strongly depolarized, though this region of  $A\beta$  was not strongly impacted by pyroglutamylation. Additional investigations on solvation properties should be conducted to probe this effect further. Nevertheless, this analysis of the solvation shell of  $A\beta$  and its pyroglutamylated forms indicates that release of these water molecules into bulk, relaxing them back to their equilibrium dipole moments, may contribute to the aggregation process. Therefore, the perturbations induced by pyroglutamylation may be an additional contributing factor in describing this process.

## 4 | CONCLUSIONS

Here, we have described the development of pyroglutamate parameters compatible with the Drude-2019 FF. The newly developed parameters were compared against QM data and were of comparable quality to previously developed parameters of other molecules [60, 25]. These parameters were subsequently used to perform simulations of pyroglutamylated  $A\beta$ .

Our results are also the first study of monomeric  $A\beta_{\text{pE3-42}}$  and  $A\beta_{\text{pE11-42}}$  carried out with a polarizable FF. We found that the pyroglutamylation at positions 3 and 11 results shifted inter-residue contacts and conformations that give rise to changes in dipole-dipole interactions. Specifically,  $A\beta_{\text{pE3-42}}$  results in shifts in the secondary structure that correspond to changes in peptide-bond dipole moment and changes in SASA. Furthermore,  $A\beta_{\text{pE3-42}}$  and  $A\beta_{\text{pE11-42}}$

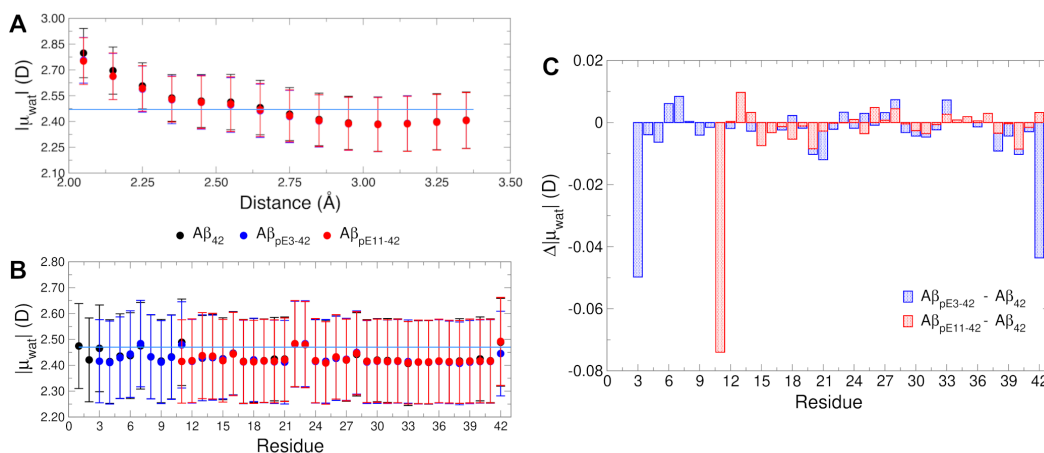


**FIGURE 8** Perturbations to water dipole moments in the first solvation shell around each peptide. (A) Average molecular dipole moments of water molecules as a function of distance away from the nearest peptide heavy atom. (B) Average molecular dipole moments of water molecules exclusively in the first solvation shell around each residue. (C) The difference in water dipole moments around each residue relative to that of the full-length  $A\beta_{42}$ . The legend shown between panels (A) and (B) applies to both panels. Error bars indicate the root-mean-square deviation of the pooled data sets. The horizontal, light blue line in panels (A) and (B) corresponds to the average bulk dipole moment of the SWM4-NDP water model (2.47 D).

adopt similar tertiary contacts that cause the hydrophobic C-terminus (residues 39-42) to interact closely with pyroglutamate at positions 3 and 11. This shift in tertiary contacts leaves much of the hydrophobic C-terminal region more solvent-exposed.

This shift in tertiary structure suggests that the modification of the N-terminus may cause  $A\beta$  to have residues that are normally solvent-occluded to become exposed, causing the peptide to become more prone to aggregating. We also note that the change in tertiary structure results in similar changes in sidechain dipole moments, highlighting that  $A\beta_{pE3-42}$  and  $A\beta_{pE11-42}$  may adopt unique microenvironments that give rise to different conformational ensembles that are sensitive to induced electronic polarization effects. Overall, we found that changes in secondary and tertiary structure are largely driven by perturbations to peptide-bond and sidechain dipole moments. These data suggest that the polar N-terminal residues 1-10 may serve to modulate the interactions among the hydrophobic regions of  $A\beta$  that lead to aggregation, and their removal via pyroglutamylation may enhance aggregation. Further, the impact of pyroglutamylation extends to mutual polarization effects between the  $A\beta$  peptides and the first solvation shell, perhaps exposing a new contributor to the forces driving aggregation of these species.

## Author Contributions

**Darcy S. Davidson:** Conceptualization; investigation; formal analysis; writing - original draft; writing - review and editing; visualization. **Justin A. Lemkul:** Funding acquisition; conceptualization; formal analysis; writing - review and editing; visualization. The final version of the article has been reviewed and approved by all authors.

## Acknowledgments

The authors thank Dr. Marcelo D. Polêto for help and advice in performing analysis and for critical review of the manuscript. The authors also thank Virginia Tech Advanced Research Computing for computing time and resources. This work was supported by the National Institutes of Health (grant R35GM133754, to J.A.L.) and the USDA-NIFA (project VA-160092).

## Conflict of Interest

The authors declare no conflict of interest.

## Data Availability Statement

The input files (coordinates, topologies, and associated force field parameter files) are available via the Open Science Framework at <https://osf.io/mqcf/>.

## references

- [1] Weggen S, Beher D. Molecular consequences of amyloid precursor protein and presenilin mutations causing autosomal-dominant Alzheimer's disease. *Alzheimer's Research and Therapy* 2012;4:9. <https://www.ncbi.nlm.nih.gov/pmc/articles/PMC3334542/pdf/alzrt107.pdf><http://alzres.biomedcentral.com/articles/10.1186/alzrt107>.
- [2] Turner PR, O'Connor K, Tate WP, Abraham WC. Roles of amyloid precursor protein and its fragments in regulating neural activity, plasticity and memory. *Progress in Neurobiology* 2003;70(1):1–32.
- [3] Sisodia SS.  $\beta$ -Amyloid precursor protein cleavage by a membrane-bound protease. *Proceedings of the National Academy of Sciences of the United States of America* 1992;89(13).
- [4] Nunan J, Small DH. Regulation of APP cleavage by  $\alpha$ -,  $\beta$ - and  $\gamma$ -secretases. *FEBS Letters* 2000;483:6–10.
- [5] Mori H, Takio K, Ogawara M, Selkoe DJ. Mass spectrometry of purified amyloid  $\beta$  protein in Alzheimer's disease. *The Journal of Biological Chemistry* 1992 8;267(24):17082–6.
- [6] Marksteiner J, Humpel C.  $\beta$ -amyloid expression, release and extracellular deposition in aged rat brain slices. *Molecular Psychiatry* 2008 10;13:939–952. <http://www.nature.com/articles/4002072>.
- [7] Dunys J, Valverde A, Checler F. Are N- And C-terminally truncated A  $\beta$  species key pathological triggers in Alzheimer's disease? *Journal of Biological Chemistry* 2018;293:15419–15428.
- [8] Jang H, Arce FT, Ramachandran S, Capone R, Azimova R, Kagan BL, et al. Truncated  $\beta$ -amyloid peptide channels provide an alternative mechanism for Alzheimer's Disease and Down syndrome. *Proceedings of the National Academy of Sciences* 2010 4;107:6538–6543.
- [9] Scheidt HA, Adler J, Krueger M, Huster D. Fibrils of truncated pyroglutamylyl-modified A $\beta$  Peptide exhibit a similar structure as wildtype mature A $\beta$  fibrils. *Scientific Reports* 2016;6.
- [10] Liu K, Solano I, Mann D, Lemere C, Mercken M, Trojanowski JQ, et al. Characterization of A $\beta$ 11-40/42 peptide deposition in Alzheimer's disease and young Down's syndrome brains: implication of N-terminally truncated A $\beta$  species in the pathogenesis of Alzheimer's disease. *Acta neuropathologica* 2006;112:163–174.
- [11] Portelius E, Bogdanovic N, Gustavsson MK, Volkman I, Brinkmalm G, Zetterberg H, et al. Mass spectrometric characterization of brain amyloid  $\beta$  isoform signatures in familial and sporadic Alzheimer's disease. *Acta Neuropathologica* 2010 8;120:185–193.

- [12] Schilling S, Lauber T, Schaupp M, Manhart S, Scheel E, Böhm G, et al. On the seeding and oligomerization of pGlu-amyloid peptides (in vitro). *Biochemistry* 2006;45(41):12393–12399.
- [13] Bridel C, Hoffmann T, Meyer A, Durieux S, Koel-Simmelnink MA, Orth M, et al. Glutaminyl cyclase activity correlates with levels of A $\beta$  peptides and mediators of angiogenesis in cerebrospinal fluid of Alzheimer's disease patients. *Alzheimer's Research and Therapy* 2017;9.
- [14] Cynis H, Scheel E, Saido TC, Schilling S, Demuth HU. Amyloidogenic processing of amyloid precursor protein: Evidence of a pivotal role of glutaminyl cyclase in generation of pyroglutamate-modified amyloid- $\beta$ . *Biochemistry* 2008;47.
- [15] Jawhar S, Wirths O, Bayer TA. Pyroglutamate Amyloid- $\beta$  (A $\beta$ ): A Hatchet Man in Alzheimer Disease. *Journal of Biological Chemistry* 2011 11;286:38825–38832. <http://www.jbc.org/lookup/doi/10.1074/jbc.R111.288308>.
- [16] Harigaya Y, Saido TC, Eckman CB, Prada CM, Shoji M, Younkin SG. Amyloid  $\beta$  protein starting pyroglutamate at position 3 is a major component of the amyloid deposits in the Alzheimer's disease brain. *Biochemical and Biophysical Research Communications* 2000;276:422–427.
- [17] He W, Barrow CJ. The A $\beta$  3-pyroglutamyl and 11-pyroglutamyl peptides found in senile plaque have greater  $\beta$ -sheet forming and aggregation propensities in vitro than full-length A $\beta$ . *Biochemistry* 1999;38.
- [18] Moro ML, Phillips AS, Gaimster K, Paul C, Mudher A, Nicoll JAR, et al. Pyroglutamate and Isoaspartate modified Amyloid- $\beta$  in ageing and Alzheimer's disease. *Acta Neuropathologica Communications* 2018;6:3.
- [19] Lemkul JA, Bevan DR. The Role of Molecular Simulations in the Development of Inhibitors of Amyloid -Peptide Aggregation for the Treatment of Alzheimer's Disease. *ACS Chemical Neuroscience* 2012;3(11):845–856. <https://doi.org/10.1021/cn300091a>, pMID: 23173066.
- [20] Strodel B. Amyloid aggregation simulations: challenges, advances and perspectives. *Current Opinion in Structural Biology* 2021;67:145–152. <https://www.sciencedirect.com/science/article/pii/S0959440X20301871>, theory and Simulation/Computational Methods Macromolecular Assemblies.
- [21] Sgourakis NG, Merced-Serrano M, Boutsidis C, Drineas P, Du Z, Wang C, et al. Atomic-Level Characterization of the Ensemble of the A $\beta$ (1–42) Monomer in Water Using Unbiased Molecular Dynamics Simulations and Spectral Algorithms. *Journal of Molecular Biology* 2011 1;405:570–583. <https://linkinghub.elsevier.com/retrieve/pii/S002228361001123x>.
- [22] Lincoff J, Sasmal S, Head-Gordon T. The combined force field-sampling problem in simulations of disordered amyloid- $\beta$  peptides. *The Journal of Chemical Physics* 2019 3;150:104108. <http://dx.doi.org/10.1063/1.5078615><http://aip.scitation.org/doi/10.1063/1.5078615>.
- [23] Gillman AL, Jang H, Lee J, Ramachandran S, Kagan BL, Nussinov R, et al. Activity and architecture of pyroglutamate-modified amyloid- $\beta$  (A $\beta$ pE3-42) pores. *Journal of Physical Chemistry B* 2014;118.
- [24] Lemkul JA, Huang J, Roux B, MacKerell Jr AD. An Empirical Polarizable Force Field Based on the Classical Drude Oscillator Model: Development History and Recent Applications. *Chemical Reviews* 2016;116:4983–5013.
- [25] Lin FY, Huang J, Pandey P, Rupakheti C, Li J, Roux B, et al. Further Optimization and Validation of the Classical Drude Polarizable Protein Force Field. *Journal of Chemical Theory and Computation* 2020;16:3221–3239.
- [26] Davidson DS, Kraus JA, Montgomery JM, Lemkul JA. Effects of Familial Alzheimer's Disease Mutations on the Folding Free Energy and Dipole–Dipole Interactions of the Amyloid  $\beta$ -Peptide. *The Journal of Physical Chemistry B* 2022;126(39):7552–7566. <https://doi.org/10.1021/acs.jpcc.2c03520>, pMID: 36150020.
- [27] Frisch MJ, Trucks GW, Schlegel HB, Scuseria GE, Robb MA, Cheeseman JR, et al., Gaussian09 Revision E.01; 2009. Gaussian Inc. Wallingford CT 2009.

- [28] Smith DGA, Burns LA, Simmonett AC, Parrish RM, Schieber MC, Galvelis R, et al. Psi4 1.4: Open-source software for high-throughput quantum chemistry. *The Journal of Chemical Physics* 2020 5;152:184108.
- [29] Brooks BR, Brooks III CL, MacKerell Jr AD, Nilsson L, Petrella RJ, Roux B, et al. CHARMM: The biomolecular simulation program. *Journal of Computational Chemistry* 2009;30(10):1545–1614.
- [30] Kirkpatrick S, Gelatt CD, Vecchi MP. Optimization by Simulated Annealing. *Science* 1983 5;220:671–680.
- [31] Ransil BJ. Studies in Molecular Structure. IV. Potential Curve for the Interaction of Two Helium Atoms in Single-Configuration LCAO MO SCF Approximation. *The Journal of Chemical Physics* 1961 6;34:2109–2118.
- [32] Boys SF, Bernardi F. The calculation of small molecular interactions by the differences of separate total energies. Some procedures with reduced errors. *Molecular Physics* 1970 10;19:553–566.
- [33] Huang J, Rauscher S, Nawrocki G, Ran T, Feig M, Groot BLD, et al. CHARMM36m: An improved force field for folded and intrinsically disordered proteins. *Nature Methods* 2016;14:71–73.
- [34] Jorgensen WL, Chandrasekhar J, Madura JD, Impey RW, Klein ML. Comparison of simple potential functions for simulating liquid water. *The Journal of Chemical Physics* 1983;79:926–935.
- [35] Neria E, Fischer S, Karplus M. Simulation of activation free energies in molecular systems. *Journal of Chemical Physics* 1996;105:1902–1921.
- [36] Durell SR, Brooks BR, Ben-naim A. Solvent-Induced Forces between Two Hydrophilic Groups. *Journal of Physical Chemistry* 1994;98:2198–2202.
- [37] Phillips JC, Braun R, Wang W, Gumbart J, Tajkhorshid E, Villa E, et al. Scalable molecular dynamics with NAMD. *J Comput Chem* 2005;26(16):1781–1802.
- [38] Martyna GJ, Tobias DJ, Klein ML. Constant pressure molecular dynamics algorithms. *The Journal of Chemical Physics* 1994;101:4177–4189.
- [39] Feller SE, Zhang Y, Pastor RW, Brooks BR. Constant pressure molecular dynamics simulation: The Langevin piston method. *The Journal of Chemical Physics* 1995;103:4613–4621.
- [40] Darden T, York D, Pedersen L. Particle mesh Ewald: An N-log(N) method for Ewald sums in large systems. *The Journal of Chemical Physics* 1993;98:10089–10092.
- [41] Essmann U, Perera L, Berkowitz ML, Darden T, Lee H, Pedersen LG. A smooth particle mesh Ewald method. *The Journal of Chemical Physics* 1995;103:8577–8593.
- [42] Ryckaert JP, Ciccotti G, Berendsen HJC. Numerical integration of the cartesian equations of motion of a system with constraints: molecular dynamics of N-alkanes. *Journal of Computational Physics* 1977;23:327–341.
- [43] Lamoureux G, Harder E, Vorobyov IV, Roux B, MacKerell Jr AD. A polarizable model of water for molecular dynamics simulations of biomolecules. *Chemical Physics Letters* 2006;418:245–249.
- [44] Jiang W, Hardy DJ, Phillips JC, MacKerell Jr AD, Schulten K, Roux B. High-performance scalable molecular dynamics simulations of a polarizable force field based on classical Drude oscillators in NAMD. *Journal of Physical Chemistry Letters* 2011;2:87–92.
- [45] Lamoureux G, Roux B. Modeling induced polarization with classical Drude oscillators: Theory and molecular dynamics simulation algorithm. *Journal of Chemical Physics* 2003;119:3025–3039.
- [46] Chowdhary J, Harder E, Lopes PEM, Huang L, MacKerell Jr AD, Roux B. A polarizable force field of dipalmitoylphosphatidylcholine based on the classical Drude model for molecular dynamics simulations of lipids. *Journal of Physical Chemistry B* 2013;117:9142–9160.

- [47] Eastman P, Swails J, Chodera JD, McGibbon RT, Zhao Y, Beauchamp KA, et al. OpenMM 7: Rapid development of high performance algorithms for molecular dynamics. *PLOS Computational Biology* 2017 7;13:e1005659. <https://dx.plos.org/10.1371/journal.pcbi.1005659>.
- [48] Huang J, Lemkul JA, Eastman PK, MacKerell Jr AD. Molecular dynamics simulations using the drude polarizable force field on GPUs with OpenMM: Implementation, validation, and benchmarks. *Journal of Computational Chemistry* 2018 8;39:1682–1689. <http://doi.wiley.com/10.1002/jcc.25339>.
- [49] Lemkul JA, Huang J, MacKerell Jr AD. Induced Dipole-Dipole Interactions Influence the Unfolding Pathways of Wild-Type and Mutant Amyloid  $\beta$ -Peptides. *The Journal of Physical Chemistry B* 2015 12;119:15574–15582. <https://pubs.acs.org/doi/10.1021/acs.jpcc.5b09978>.
- [50] Abraham MJ, Murtola T, Schulz R, Páll S, Smith JC, Hess B, et al. GROMACS: High performance molecular simulations through multi-level parallelism from laptops to supercomputers. *SoftwareX* 2015;1-2:19–25.
- [51] Broersen K, Rousseau F, Schymkowitz J. The culprit behind amyloid beta peptide related neurotoxicity in Alzheimer's disease: oligomer size or conformation? *Alzheimer's Research & Therapy* 2010;2:12.
- [52] Kirkitadze MD, Condrón MM, Teplow DB. Identification and characterization of key kinetic intermediates in amyloid  $\beta$ -protein fibrillogenesis. *Journal of Molecular Biology* 2001 10;312:1103–1119.
- [53] Nath S, Buell AK, Barz B. Pyroglutamate-modified amyloid  $\beta$ (3-42) monomer has more  $\beta$ -sheet content than the amyloid  $\beta$ (1-42) monomer. *Physical Chemistry Chemical Physics* 2023;25:16483–16491.
- [54] Huang J, MacKerell Jr AD. Induction of peptide bond dipoles drives cooperative helix formation in the (AAQAA)<sub>3</sub> peptide. *Biophysical Journal* 2014;107:991–997. <http://dx.doi.org/10.1016/j.bpj.2014.06.038>.
- [55] Ahmed MC, Papaleo E, Lindorff-Larsen K. How well do force fields capture the strength of salt bridges in proteins? *PeerJ* 2018;6:e4967.
- [56] Dobson CM. Protein-misfolding diseases: Getting out of shape. *Nature* 2002 8;418:729–730.
- [57] Wada A. The  $\alpha$ -helix as an electric macro-dipole. *Adv Biophys* 1976;p. 1–63.
- [58] Guo H, Karplus M. Solvent Influence on the Stability of the Peptide Hydrogen Bond: A Supramolecular Cooperative Effect. *The Journal of Physical Chemistry* 1994 07;98(29):7104–7105.
- [59] Ngo VA, Fanning JK, Noskov SY. Comparative Analysis of Protein Hydration from MD simulations with Additive and Polarizable Force Fields. *Advanced Theory and Simulations* 2019;2(2):1800106. <https://onlinelibrary.wiley.com/doi/abs/10.1002/adts.201800106>.
- [60] Lemkul JA, MacKerell Jr AD. Polarizable Force Field for DNA Based on the Classical Drude Oscillator: I. Refinement Using Quantum Mechanical Base Stacking and Conformational Energetics. *Journal of Chemical Theory and Computation* 2017;13.